Multi-Frequency Broadband Vibration Mitigation of a Beam Under Tensile Load

Marcela Machado (marcelam@unb.br)
University of Brasilia: Universidade de Brasilia https://orcid.org/0000-0002-7488-7201
Maciej Dutkiewicz
Uniwersytet Kazimierza Wielkiego w Bydgoszczy

Research Article

Keywords: Metamaterial, Rainbow metamaterial, Digital Twin, Conductor cable, Bayesian identification

Posted Date: January 11th, 2022

DOI: https://doi.org/10.21203/rs.3.rs-1211676/v1

Multi-frequency broadband vibration mitigation of a beam under tensile load

Marcela R. Machado[1*] and Maciej Dutkiewicz[2†]

[1*]Department of Mechanical Engineering, University of Brasilia, Campus Universitário Darcy Ribeiro, Brasilia, 70910-900, Federal District, Brasil.

[2]Faculty of Civil, Environmental Engineering and Architecture, University of Science and Technology, Al. Prof. Sylwestra Kaliskiego 7, Bydgoszcz, ,85-796, Poland.

*Corresponding author(s). E-mail(s): marcelam@unb.br;
Contributing authors: macdut@pbs.edu.pl;
†These authors contributed equally to this work.

Abstract

The vibration characterization is directly associated with the system's physical properties, such as mass, damping, and stiffness. For over a century, vibration resonator or dynamic absorber has been used for vibration control and mitigation in many sectors of engineering. A limitation of this device is that it acts as a notch filter, which is only effective over a narrow band of frequencies. Therefore, researchers have designed the call metamaterial, which in this case, targets the improvement of vibration attenuation and induces locally resonant bandgaps. This work investigates the broadband vibration mitigation of a beam under tensile load with periodically attached dynamic absorbers. The study uses the modal analysis approach, a simple formulation that only depends on the resonator target frequency and total mass ratio to investigate single and multiple-frequency bandgap formation. Metamaterial and rainbow metamaterial beam under tensile load are employed to widen the gap. In practical designs, a finite number of resonators is required for the open bandgap, and this ideal number is explored in the paper. Additionally, a tensiled beam (cable) virtual twin is built from a physical system to forecast its broadband vibration mitigation with the metamaterial approach. Numerical investigations are conducted regarding the effects of mass ratio

and the ideal mass ratio on the open and on the gap convergence, as well as resonators in single and multiple arrangements inducing multiple gaps.

Keywords: Metamaterial, Rainbow metamaterial, Digital Twin, Conductor cable, Bayesian identification

1 Introduction

The design and development of metamaterial for engineering applications has grown over the decade thanks to advances in the manufacturing process. The application of metamaterials in general, including electromagnetic, optical, and acoustic implementations is present in a variety of economy sectors, as shown by a recent study published by Grand View Research. It estimates that the metamaterial market will be worth 4,634.8 Million USD by 2025 [5]. Noise and vibration cause fatigue and subsequent mechanical and structural failures that can lead to accidents, system degradation, human discomfort, and catastrophic failures. Targeting this problem, metamaterials offers a large application in vibration control, from attenuating vibration to inducing an isolation and mitigation broadband, known as bandgaps. The metastructure design to control the vibration concept, as a structure attached to a periodical number of discrete spring-mass-damper absorbers, proved to be an efficient design in application aiming to vibration broadband control that works also for elastic waves of short and long wavelengths[4].

A comprehensive overview of materials and their applications was published by [6] while [7] explored metamaterials for vibration control. Local resonators (LR) is based on the concept of mechanical dynamic vibration absorbers (DVAs) [1, 8]. Several researchers have explored the functionality and efficiently of locally resonant elastic-acoustic metamaterials on a variety of structures. The theory of metamaterial beam designed for broadband vibration control was published in [8], and Dianlong et. al. [10] explored the flexural vibration band gaps in Euler-Bernoulli beams with locally resonant structures with two degrees of freedom. The mechanism of bandgap formation in a beam was presented in Sugino et. al.[13] and a general theory for bandgap estimation in locally resonant metastructures was published in [12]. Xiao et al.[9, 11] investigated the bandgap behaviour and the formation mechanisms of beams with periodically attached vibration absorbers and, in [16], the authors expanded on previous studies by introducing multiple periodic arrays of local resonators into a LR beam to explore the broadband vibration attenuation. Timoshenko beams attached with single- and multi-resonator were investigated in [14, 15]. Instabilities and non-linearities in locally resonant metamaterial beam were investigated in [27, 28].

Aside from the numerical methods commonly used to analyze the metamaterials, e.g. finite element method, spectral element method, plane wave expansion, wave finite elements, among others, Sugino et al. [12, 13] proposed

an analytical solution based on the modal analysis of bandgap formation. The modal analysis approach [1, 19] incorporates the modal parameter information and the dependence of the bandgap width on the number and spatial distribution of attachments in a finite structure. In this case, lattice-based dispersion characteristics of local resonator and the modal interaction between a primary structure and its attachments is covered by [12]. The authors managed to derive (in closed form) the expression for the bandgap edge frequencies using the resonant frequency of the resonators and the ratio of the resonator mass to the plain structure mass. This technique has been used in structures as strings, rods, shafts, bare beams, membranes, and plates. Zhong et al. [40] investigated the metamaterial I-Girder beam for vibration absorption of composite stayed bridges and Singleton et al.[41] designed a resonator-based metamaterial for broadband control of transverse taut string vibration. Zhou et al[29] also investigated the tunable flexural wave band gaps in a prestressed elastic beam with periodic smart resonators.

A practical application involving beam under tensile load system is the cable structures. The mathematical model of the cable conductor available in the literature goes to the simplest mathematical based on the taut strings without bending stiffness to more complex where a homogeneous elastic beam with constant bending stiffness and subjected to a constant tensile load is considered [20–22]. A review of the mechanical models of cables was published by Cardou [23] and Spak et al. [24, 25]. The stockbridge damper is a tuned mass damper commonly used for vibration suppression in conductor cable. The control is over one to two resonant frequencies and its effectiveness can be affected by the installation position on the conductor and overall characteristics [26]. The concept of the Stockbridge damper is similar to the local resonators that were thoroughly investigated on the acoustic metamaterial used to induce bandgaps. Digital twin technology is an emerging concept whose application has gained prevalence in the industry and academia [35]. A digital twin is a computed model of a physical device or system that represents all functional features and continually adapts to operational changes based on the collected online data and information. It can also forecast the future of the corresponding physical counterpart [34, 36]. Despite numerous applications and models exploring vibration control on the beam under tensile load system (cables), to date, studies on the metamaterial and rainbow metamaterial beam under tensile load exploring their dynamic response and the broadband bandgap formation in single to multiple frequencies are still unheard of in the literature.

This paper proposes a metamaterial beam under tensile load to induce single- and multiple-frequency local bandgap formation and a efficient way to wide them. Modal analysis approach is used based on the available theory present in [12] is extended to a beam under tensile load and multi-frequency frameworks. The objectives of the present study are to address three major issues: (i) formulating the modal analysis of single and multiple bandgap formation to a beam under tensile load; (ii) investigating the efficiency of metamaterial and the rainbow metamaterial to broadband gap widening related to

the ideal mass ratio; and (iii) demonstrating the application of the broadband vibration mitigation in a real system by applying the concept of the digital twin. The metamaterial' numerical models would be developed based on the analytical modal analysis to carry out an accurate yet computationally efficient analysis. The cable's digital twin run from the physical system to forecast its broadband vibration mitigation and associated implication.

2 Beam under tensile load

Analytical solution of vibrations in a beam under effect of tensile load and other external forces $f(x,t)$ that induces lateral vibrations illustrated in Fig. 1a was formulated in Rao[3]. Free-body diagram of an infinitesimal element draft is shown in Fig. 1b, the external forces per unit length are the bending moment, $M(x,t)$, shear force $V(x,t)$, and axial or tensile load $T(x,t)$.

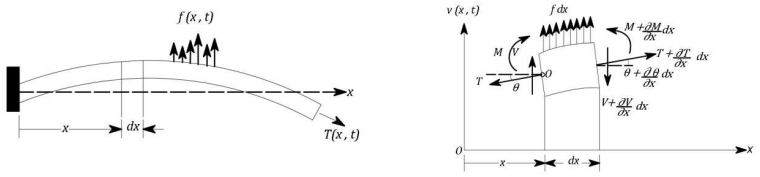

(a) (b)

Fig. 1: Slender flexural beam under tensile load effect(a) and infinitesimal element (b) [3].

Applying the dynamic equilibrium equation, the vertical motion is

$$-(V+dV)+fdx+V+(T+dT)\sin(\theta+d\theta)-T\sin\theta=\rho A\,dx\frac{\partial^2 w}{\partial t^2} \quad (1)$$

where $dV = \partial\ V/\partial\ x\ dx$, A is the cross-section area, ρ the material mass density, w and θ are the vertical and the rotational displacements, respectively. The motion equation around the point O is expressed by

$$(M+dM)-(V+dV)\,dx+fdx\frac{dx}{2}-M=0 \quad (2)$$

where $dM = \partial\ M/\partial\ x\ dx$. By using the relationship $V = \partial\ M/\partial\ x\ dx$ and from the Euler-Bernoulli thin beam theory, the relationship between bending moment and deflection yields

$$M=EI\frac{\partial^2 w}{\partial x^2} \quad (3)$$

where E is the elastic modulus and I is the moment of inertia. Assuming small displacement and combining Eqs. (1) and (2), the tensioned beam's differential equation of motion will be

$$\frac{\partial^2}{\partial x^2}\left[EI\frac{\partial^2 w}{\partial x^2}\right] + \rho A\frac{\partial^2 w}{\partial t^2} - T\frac{\partial^2 w}{\partial x^2} = f\left(x,t\right) \tag{4}$$

or in the homogeneous form

$$EI\frac{\partial^4 w\left(x,t\right)}{\partial x^4} - T\frac{\partial^2 w\left(x,t\right)}{\partial x^2} + \rho A\frac{\partial^2 w\left(x,t\right)}{\partial t^2} = 0 \tag{5}$$

The solution of Eq. (5) can be obtained via separation of variables technique. Assuming harmonic solution $w(x,t) = w(x)(A\ cos\ \omega\ t\ +\ B\ sin\ \omega\ t)$, where $w(x) = C^{sx}$. For a simply supported beam under axial force, the natural frequency can be written as

$$\omega_n = \frac{\pi^2}{L^2}\sqrt{\frac{EI}{\rho A}}\left(n^4 + \frac{n^2 TL^2}{\pi^2 EI}\right)^{\frac{1}{2}}, \qquad n = 1, 2, \ldots\ . \tag{6}$$

and modal shape

$$\phi_n = \sin(n\pi x/L) \tag{7}$$

where $\rho\ A$ is the mass per unit of length, EI is the uniform bending rigidity, L is the cable length, and (x,t) is the tensioned beam displacement as a function of the position x and time t.

3 Modal analysis of bandgap formation in a beam under tensile load

Applying the assumption of an infinite number of resonators placed on the structure, the locally resonant bandgap edge frequencies are derived in closed form. This expression for the bandgap edge frequencies only depends on the resonant frequency of the resonators and the ratio of resonator mass to plain structure mass, and it can be used for any typical vibrating structure (strings, rods, shafts, beams, membranes, or plates). To tie this work to other research in the field, the bandgap expression is validated numerically with the band structure obtained from the plane wave expansion method. To demonstrate that the derived bandgap expression is useful for design, we validate the bandgap expression for a finite number of uniformly distributed resonators. We also discuss the performance of metastructures with non-uniform resonator distributions, as well as the effect of parameter variation in the resonant frequencies of the resonators.

3.1 Single frequency bandgap formation

The general equation of motion of a forced, undamped system with distributed parameters is of the form of [1]

$$\mathcal{L}(x)w(x,t) + m\ddot{w}(x,t) - \sum_{p=1}^{S} k_p u_p(t)\delta(x - x_p) = f(x,t) \tag{8}$$

where $m = \rho A$ is the mass per unit of length and, for the beam under tensile load, the stiffness operator is

$$\mathcal{L} = \frac{d^2}{dx^2}\left[EI\frac{d^2w}{dx^2}\right] - T\frac{d^2w}{dx^2}$$

The equation for the resonators yields

$$m_p\ddot{u}_p(t) + k_p u_p(t) + m_p\ddot{w}(x,p,t) = 0 \quad p = 1,2,...,S. \tag{9}$$

where $w(x,p,t)$ is the displacement of a point with position vector p related to the beam, $\mathcal{L}$ is the linear homogeneous stiffness differential operator, m is the mass density of the structure, k_p, m_p, and $u_p(t)$ are, respectively, the stiffness, mass, and displacement of the pth resonator, x_p is the attachment location of the pth resonator, $\delta(x - x_p)$ is the spatial Dirac delta function, S is the total number of resonators, and $f(x,t)$ is the external force. The $\dot{}$ denotes the partial differentiation with respect to time. The general solution of the Eq.(8) of the form,

$$w(x,t) = \sum_{j=1}^{N} \phi_j(x)y_j(t) \tag{10}$$

by replacing Eq.(10) into Eq.(8) gives

$$\sum_{j=1}^{N} \mathcal{L}(x)\phi_j(x)y_j(t) + m\sum_{j=1}^{N} \phi_j(x)\ddot{y}_j(t) - \sum_{p=1}^{S} k_p u_p(t)\delta(x - x_p) = f(x,t) \tag{11}$$

The normalized mode shape of the bare structures satisfy the orthogonality condition [1],

$$\int_0^L m\phi_j(x)\phi_i(x)dx = \delta_{ij} = 1$$
$$\int_0^L \mathcal{L}(x)\phi_j(x)\phi_i(x)dx = \omega_j^2\delta_{ij}$$

where $phi_j(x)$ and $\phi_i(x)$ are the j-th and i-th normalized mode shapes of the bare structure, δ_{ij} is the Kronecker delta, and ω_j^2 is the resonant frequency of

the j-th mode of the bare structure. Multiplying Eq. (11) by $\phi_i(x)$ and applying the orthogonality conditions of the mode shapes gives

$$\ddot{y}_j(t) + \omega_j^2 y_j(t) - \sum_{p=1}^{S} k_p u_p(t)\phi_j(xp) = q_j(t) \tag{12}$$

where $q_j(t) = \int_0^L \phi_i(x) f(x,t)dx$. Assuming $y_j(t) = Y_j e^{i\omega t}$, $u_p(t) = U_p e^{i\omega t}$, $f(x,t) = F\delta(x - x_p)e^{i\omega t}$, $Q_j = F\phi_j(xe)$, and substituting those variables in Eq. (12) yields

$$(\omega_j^2 - \omega^2)Y_j - \sum_{p=1}^{S} k_p U_p \phi_j(xp) = Q_j \tag{13}$$

with the general solution in Eq. (9), one has

$$-\omega^2 m_p U_p + k_p Up - \omega^2 m_p \sum_{i=1}^{N} \phi_i(xp) Y_i = 0 \tag{14}$$

and

$$U_p = \frac{\omega^2 m_p}{k_p - \omega^2 m_p} \sum_{i=1}^{N} \phi_i(xp) Y_i \tag{15}$$

Replacing Eq. (15) in (13) expresses the bare beam coupled to the resonators in a modal base as

$$(\omega_i^2 - \omega^2)Y_j - \sum_{p=1}^{S} k_p \phi_j(xp) \frac{\omega^2}{\omega_p^2 - \omega^2} \sum_{i=1}^{N} \phi_i(xp) Y_i = Q_j \tag{16}$$

where $\omega_p^2 = k_p/m_p$, for $m_p = \epsilon m \Delta L$[2], for $\Delta L_j = \int_{L_j} dL$ is the length of the subdomain L_j, therefore Eq. (13) becomes

$$(\omega_i^2 - \omega^2)Y_j - \sum_{p=1}^{S} -\epsilon m \Delta L \omega_p^2 \phi_j(xp) \frac{\omega^2}{\omega_p^2 - \omega^2} \sum_{i=1}^{N} \phi_i(xp) Y_i = Q_j \tag{17}$$

rearranging Eq.(17) yields in a system equation of N coupled linear equations that cannot be solved for a simple analytical expression due to the coupling introduced by absorbers[2]. This case requires a numerical solution for the response of a given system.

$$\begin{aligned}
&(\omega_i^2 - \omega^2)Y_j - \epsilon\omega^2 \sum_{i=1}^{N} \sum_{p=1}^{S} \frac{\omega_p^2}{\omega_p^2 - \omega^2} m\phi_j(xp)\phi_i(xp)\Delta L Y_i = Q_j \\
&(\omega_i^2 - \omega^2)Y_j - \epsilon\omega^2 \sum_{i=1}^{N} \frac{\omega_p^2}{\omega_p^2 - \omega^2} \left(\sum_{p=1}^{S} m\phi_j(xp)\phi_i(xp)\Delta L \right) Y_i = Q_j
\end{aligned} \tag{18}$$

A simplification proposed by Sugino et al.[2] of the system given in Eq. (18) relies on the consideration that $S \to \infty$ while mass ratio m is kept unchanged. The domain region becomes infinitesimal and the resonators scatter throughout the entire domain, so that

$$\lim_{S\to\infty} \sum_{p=1}^{S} m\phi_j(xp)\phi_i(xp)\Delta L \approx \int_0^L m\phi_j(x)\phi_i(x)dx = \delta_{ij} \tag{19}$$

Hence, the simplification proposed in Eq. (19) is exact when $S \to \infty$, but can be used as a good approximations considering

$$\sum_{p=1}^{S} m_j\phi_j(xp)\phi_i(xp) \approx m \int_0^L m\phi_j(x)\phi_i(x)dx = m\delta_{ij} \tag{20}$$

this approximation is crucial for bandgap formation with a finite number of resonators, which become continuous in space with the assumption. Assuming the limits established in Eq. (20), Eq. (18) turn into

$$(\omega_j^2 - \omega^2)Y_j - \epsilon\omega^2 \frac{\omega^2}{\omega_p^2 - \omega^2} Y_j = Q_j \tag{21}$$

where the displacement in a modal base is given by

$$Y_i = \frac{Q_j}{(\omega_j^2 - \omega^2) - \epsilon\omega^2 \dfrac{\omega^2}{\omega_p^2 - \omega^2}} \tag{22}$$

The system of equations decouples and yields the transfer matrix of the bare structure coupled to resonators, given as

$$\alpha(\omega) = \frac{w(x_r,\omega)}{f(x_e,\omega)} = \sum_{j=1}^{N} \frac{\phi_j(x_r)\phi_j(x_e)}{\omega_j^2 - \omega^2\left(1 + \epsilon\frac{\omega_p^2}{\omega_p^2 - \omega^2}\right)} \tag{23}$$

Modal parameters of a beam under tensile load are described in section 2, Eqs. (6) and (7).

3.2 Multi-frequency bandgap formation

The general equation of motion for the beam under tensile load, attached to multiple periodic arrays of spring-mass local resonators, is of the form of

$$\mathcal{L}(x)w(x,t) + m\ddot{w}(x,t) - \sum_{\bar{n}=1}^{\bar{N}} \sum_{p=1}^{S} k_p^{\bar{n}} u_p^{\bar{n}}(t)\delta(x - x_p) = f(x,t) \tag{24}$$

where $\mathcal{L}(x)w(x,t)$ is the stiffness operator described in Eq. 9, and $w(x,p,t)$ is the displacement of a point with position vector p, m is the main structure mass. For multiple periodic arrays of attached single-DOF spring-mass local resonators, the $\delta(x-x_p)$ is the Dirac delta function. The equations for the $\bar{n}-$resonators are expressed by

$$\begin{aligned}
&m_p^{(1)}\ddot{u}_p^{(1)}(t) + k_p^{(1)}u_p^{(1)}(t) + m_p\ddot{w}(x,p,t) = 0\\
&m_p^{(2)}\ddot{u}_p^{(2)}(t) + k_p^{(2)}[u_p^{(2)}(t) - u_p^{(1)}(t)] + k_p^{(3)}[u_p^{(3)}(t) - u_p^{(2)}(t)] = 0\\
&\vdots\\
&m_p^{(\bar{n})}\ddot{u}_p^{(\bar{n})}(t) + k_p^{(\bar{n})}[u_p^{(\bar{n})}(t) - u_p^{(\bar{n}-1)}(t)] = 0 \quad p = 1,2,...,S, \quad \bar{n} = 1,2,...,\bar{N}
\end{aligned} \tag{25}$$

where $k_p^{\bar{n}}$, $m_p^{\bar{n}}$, and $u_p^{\bar{n}}(t)$ are, respectively, the stiffness, mass, and displacement of the pth resonator at $\bar{n}$-DOF, x_p is the attachment location of the pth resonator, $\delta(x-x_p)$ is the spatial Dirac delta function, S is the total number of resonators, $\bar{N}$ is the total number of degree of freedom. Similar assumptions made in section 3.1 are validated here, and the general solution presented in Eq. (10) into Eq.(24) gives

$$\sum_{j=1}^{N}\mathcal{L}(x)\phi_j(x)y_j(t) + m\sum_{j=1}^{N}\phi_j(x)\ddot{y}_j(t) - \sum_{\bar{n}=1}^{\bar{N}}\sum_{p=1}^{S}k_p^{\bar{n}}u_p^{\bar{n}}(t)\delta(x-x_p) = f(x,t) \tag{26}$$

Multiplying Eq. (26) by the normalized mode shapes $\phi_i(x)$ and applying the orthogonality conditions, the equation of motion became

$$\ddot{y}_j(t) + \omega_j^2 y_j(t) - \sum_{\bar{n}=1}^{\bar{N}}\sum_{p=1}^{S}k_p^{\bar{n}}u_p^{\bar{n}}(t)\phi_j(x_p) = q_j(t) \tag{27}$$

as expressed in section 3.1, $q_j(t)$ is the modal force, $y_j(t)$ and $u_p(t)$ assume harmonica solution, $Q_j = F\phi_j(xe)$, and substituting Eq. (12) yields

$$(\omega_j^2 - \omega^2)Y_j - \sum_{\bar{n}=1}^{\bar{N}}\sum_{p=1}^{S}k_p^{\bar{n}}U_p^{\bar{n}}\phi_j(xp) = Q_j \tag{28}$$

the multiple resonators' general solution in Eq. (25) under modal basis is expressed as

$$-\sum_{\bar{n}=1}^{\bar{N}}\omega^2 m_p^{\bar{n}}U_p^{\bar{n}} + k_p^{\bar{n}}U_p^{\bar{n}} - \omega^2 m_p^{\bar{n}}\sum_{i=1}^{N}\phi_i(x_p)Y_j = 0 \tag{29}$$

and the modal displacement as

$$U_p^{\bar{n}} = \frac{\omega^2 m_p^{\bar{n}}}{k_p^{\bar{n}} - \omega^2 m_p^{\bar{n}}} \sum_{i=1}^{N} \phi_i(x_p) Y_j \tag{30}$$

Substituting Eq. (30) into (28) it gives the beam attached to multiples resonator in a modal base solution. Thus, the main structure coupled to the multiple resonators is then

$$(\omega_i^2 - \omega^2) Y_j - \sum_{\bar{n}=1}^{\bar{N}} \sum_{p=1}^{S} k_p^{\bar{n}} \phi_j(x_p) \frac{\omega^2}{(\omega_p^{\bar{n}})^2 - \omega^2} \sum_{i=1}^{N} \phi_i(x_p) Y_j = Q_j \tag{31}$$

Assuming similar arrangement, simplification, and orthogonality properties described from Eq (16) to (20), one has

$$(\omega_j^2 - \omega^2) Y_j - Y_j \sum_{\bar{n}=1}^{\bar{N}} \epsilon^{\bar{n}} \omega^2 \frac{\omega^2}{(\omega_p^{\bar{n}})^2 - \omega^2} = Q_j \tag{32}$$

where the displacement in a modal base is represented by

$$Y_i = \frac{Q_j}{(\omega_j^2 - \omega^2) - \sum_{\bar{n}=1}^{\bar{N}} \epsilon^{\bar{n}} \omega^2 \frac{\omega^2}{(\omega_p^{\bar{n}})^2 - \omega^2}} \tag{33}$$

The system of decoupled equations return the metamaterial beam transfer matrix as

$$\alpha(\omega) = \frac{w(x_r, \omega)}{f(x_e, \omega)} = \sum_{j=1}^{N} \frac{\phi_j(x_r)\phi_j(x_e)}{\omega_j^2 - \omega^2 \left(1 + \sum_{\bar{n}=1}^{\bar{N}} \epsilon^{\bar{n}} \frac{\omega_p^2}{(\omega_p^{\bar{n}})^2 - \omega^2}\right)} \tag{34}$$

4 Numerical application

This section first explores a numerical application on the broadband bandgap formation. These studies investigate an ideal number of resonators on the single- and multi-frequency local bandgap formation. A digital twin is then performed from an experimental application of an overhead transmission conductor. From the digital twin investigations on broadband vibration, mitigation is performed.

The numerical analyses consider an aluminum beam simply supported at both ends and whose properties are: diameter of 50 mm, mass per unit length of $\rho A = 1.305$ kg/m, flexural rigidity of $EI = 1472$ Nm^2, tensile load of T = 2700 Kgf, and span of L=20 m. Figure 2 shows the metamaterial beam under tensile load designed to mitigate vibration in a single (Fig 2a) and multiple

(Fig 2b) frequency band. A unitary excitation force is located at the right edge (interface point-0), and the receptance responses estimated along the beam's interface are guided by the point from 0 to 10.

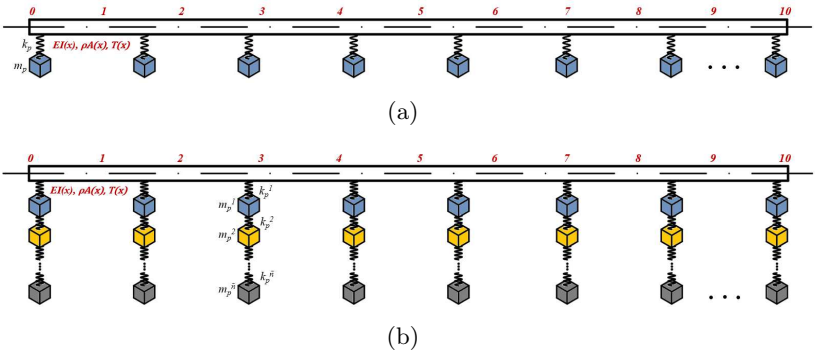

Fig. 2: Slender flexural metamaterial beam under tensile load designed to mitigate vibration in (a) single frequency and (b) multi-frequency.

This study analyzes the beam with and without control receptance response estimated at point-10 with unitary excitation force located at point-0. The resonators are designed to vibrate at 4.92 and 19.92 Hz, similar resonant frequency of the beam's 4th and 11th vibration mode shape, respectively. Figure 3 shows the control effect performed by attaching the resonators in a periodical arrangement. In those cases, the mass ratio is $\epsilon = 50\%$. Figures 3a and 3c show the receptance responses of the resonators at each desired frequency. Figures 3b and 3d are the dynamic responses of the bare and metamaterial beam. A single LR-bandgap opens around the designed frequencies. The bandgap width induces a broadband vibration band isolation. Therefore, neither the energy nor the elastic wave can propagate within the bandgap region. Moreover, wave energy is reflected or temporarily stored in resonators, which isolates the vibration in a local frequency. The control beam's dynamic response shows new resonance pick or a shift on the pick towards the neighbour modes; the result of shifting the resonance response spectrum is caused by changing the time of the shock. Similar behaviour was observed in the shock response spectrum.

Figure 4 shows the results of three cases regarding multi-frequency isolation that allows simultaneous vibration mitigation on multiple mode shapes. The first case, LR-bandgap formation, happens at 4.92 and 19.92 Hz and is shown in Fig 4a. In both frequency ranges, the vibration was mitigated, two shifting resonance picks appeared at 5.7 and 24.5Hz, and no disturbance on the other mode shapes occurred because of the LR-gap property, as shown in Fig 4b. Acoustic metamaterial relies on the infinite-resonator concept that considers the simple bandgap expression is exact when $S \longrightarrow \infty$. However, in practical applications, S will assume a finite number. The mass ratio directly affects the attenuation bandwidth, which saturates and cannot be widened by increasing

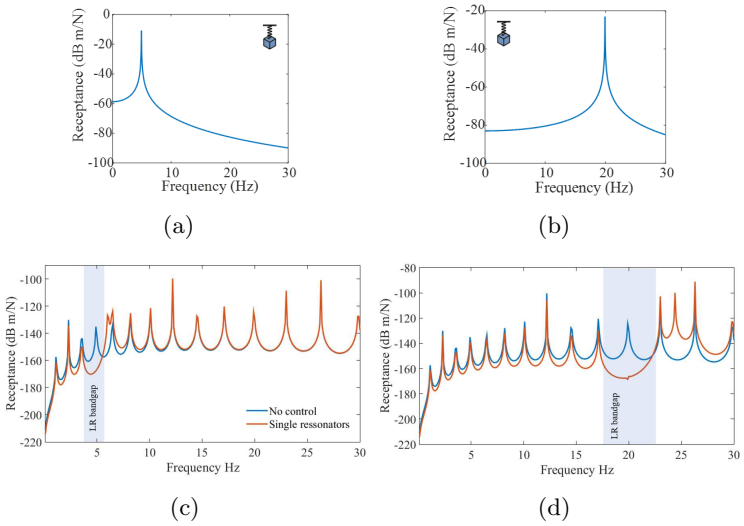

Fig. 3: Receptance responses of the resonators with natural frequencies set at (a) 4.92 Hz and (b) 19.92Hz; responses of the bare and metamaterial beam with induced bandgap at (c) 4.92 Hz and (d) 19.92Hz.

the mass. Once it is the desire to widen the bandwidth, the use of graded or rainbow metamaterial [30, 31] is an alternative. Both techniques refer to the variation in the natural frequencies of the local resonators that act together in a close range. In graded metamaterial, the resonator's mass remains the same and the stiffness changes its values to achieve the designed resonate frequency and, in a rainbow metamaterial, the resonators are developed to vibrate in specific frequency without limitation of the structural parameters. Hence, the second study case investigates the rainbow metamaterial beam under tensile load LR-bandgap widening.

Figure 4c is the resonator's response designed at frequencies 4.72, 4.82, 4.92, 5.02, and 5.12 Hz, and Fig 4e is the resonators resonating simultaneously at 19.72, 19.82, 19.903, 20.02, and 20.12 Hz. Figure 4d shows the receptance response for the bare beam, the metamaterial beam, and the rainbow metamaterial beam with the bandwidth gap given in each case. It is notorious that the rainbow metamaterial can wide the bandgap region. The shifting resonance picks emerge at 9.2Hz. Analogous receptance responses comparison, but with the LR-bandgap induce at around 19.92 Hz, is exhibited in Fig 4d. Given the rainbow multi-frequency configuration, the bandwidth does not affect the position of this gap because the resonant behaviour of local absorbers dominates such a resonance gap, but it affects the mode neighbourhood, induces an amplitude vibration reduction, and dissipates the shifting frequency.

The receptance response is estimated along with the bare and controlled beam's interface (point 0-10) with unitary excitation force located at point -0. Figure 5a shows the receptance responses map of the beam without control

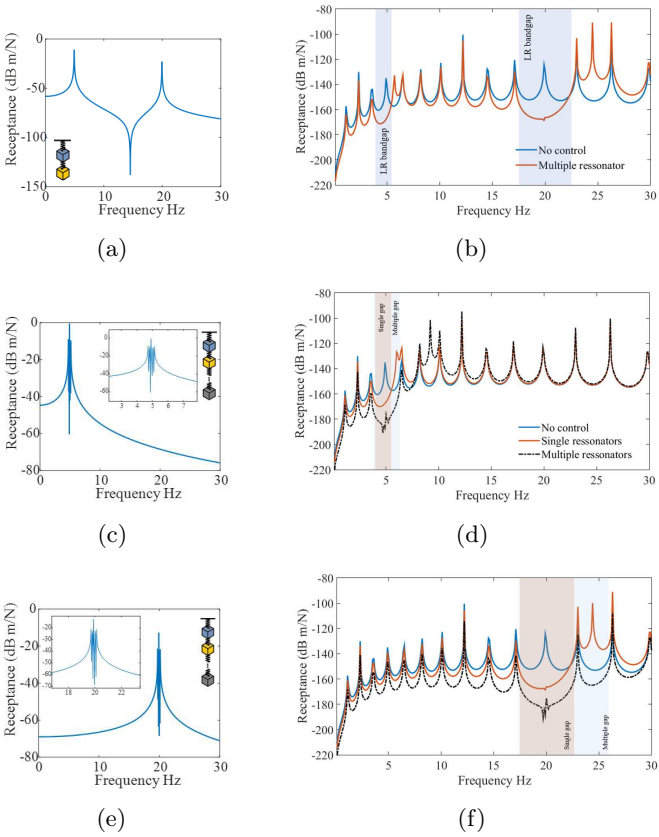

Fig. 4: Receptance responses of the resonators with natural frequencies set at (a) 4.92 and 19.92Hz; (b) Responses of the bare and metamaterial beam with induced bandgap at 4.92 and 19.92Hz; (c) Rainbow resonator receptance response with tuned frequencies around 4.92 Hz; (d) Responses of the bare, metamaterial, and rainbow metamaterial beam with induced bandgap around 4.92. (e) Rainbow resonator receptance response with tuned frequencies around 19.92 Hz; (f) Responses of the bare and metamaterial beam with induced bandgap at 4.92 and 19.92Hz.

obtained over the beam's interface, the red marks on the map represent the highest amplitude of each mode resonance pick and the blue area is the valley representing anti-resonance, or the bandwidth gap. From Fig 5b to 5f are the maps of the controlled beam. In those cases, LR-bandgap opening at similar resonators' tuned frequencies is evident and remain along with the map. For the multiple frequencies, mitigation displayed in Fig 5b opening bandgaps are simultaneous at 4.92 and 19.92 Hz. One can also see the shifting resonance frequencies towards the neighbourhood modes. By comparing metamaterial and rainbow metamaterial beam map response for a tuned resonator at 4.92Hz,

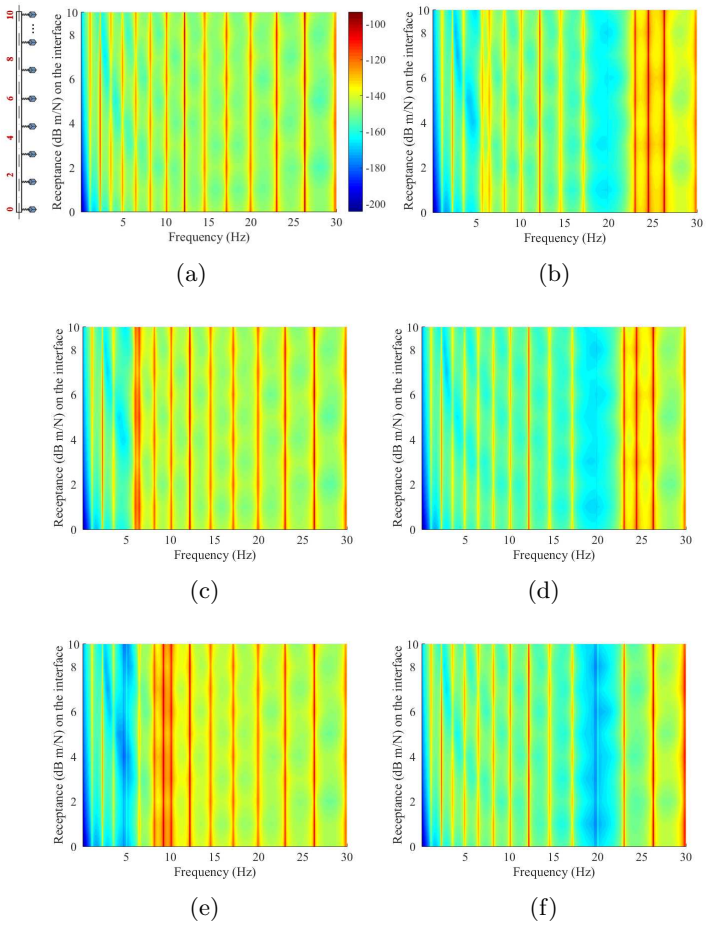

Fig. 5: Receptance map response for:(a) Bare beam; (b) Multi-frequency metamaterial beam with tuned frequencies at 4.92 and 19.92Hz; (c) Metamaterial beam with tuned frequency at 4.92Hz; (d) Metamaterial beam with tuned frequency at 19.92 Hz; (e) Rainbow metamaterial beam with tuned frequencies around 4.92Hz; (f) Rainbow metamaterial beam with tuned frequencies around 19.92Hz.

the gain in bandwidth and valley amplitude is evident on the rainbow beam and the disorder of shifting frequency input on close mode shapes (Figs 5c and 5e). Analogous behaviours are seen in Figs 5d and 5f, which are the map response for a tuned resonator at 19.92Hz. Those studies demonstrate the efficiency of both metamaterials on mitigating vibration and the LR-bandgap formation. The bandgap attenuating and isolating vibration in a frequency region also induces other resonance frequencies near the isolating frequency band region. Therefore, it is a common problem induced by vibration control based on

dynamic vibration absorbers that can be manipulated in some frequency range with the rainbow metamaterial.

4.1 Ideal mass ratio on bandgap formation

The infinite-resonator approximation described in Eq. 20 is exactly when $S \longrightarrow \infty$. Therefore, the ideal number of resonators in most applications does not rely on such conditions. In preview analyses, we investigated an efficient design of metamaterial beam under tensile load. Here the ideal number of resonators related to the mass ratio is investigated to show the bandwidth gap changes with a reduced number of ϵ. It is also important to understand how the required mass ratio attachments change target frequency and the neighbour modes. Since the beam under tensile load is uniform, the mass of each resonator is expressed as $m_p = mL/S$. Figures 6a to 6d show a map relating receptance response with the mass ratio and properly demonstrate the nature of bandgap formation in a finite structure.

In all cases, the bandgap is indicated by black dashed lines. Bandgap formation of the metamaterial beam with designed LR bandgap at 4.92Hz initiated in 10% of ratio mass and converges its bandwidth at around 50%, when its largest broadband remains this size regardless of the ratio mass addition. The rainbow metamaterial beam presented a mass ratio reduction up to the convergence, which occurs in 20% of cases (Fig 6b). The mitigation in higher modes required more mass attached to the main system for bandwidth convergence. Figure 6c is the metamaterial beam and Fig 6d the rainbow metamaterial, both considerations render a bandwidth gap convergence at 65 and 30% of ratio mass, respectively. A bandgap formation map of multi-frequency metamaterial beam tuned at 4.92 and 19.92Hz is shown in Fig 6e, which converges the bandwidth around 50 and 65% mass ratio. Without exception, the shifting resonance frequency effect is observed in the form of a red line vertically crossing the map, varying its mode shape position as the mass ratio increases.

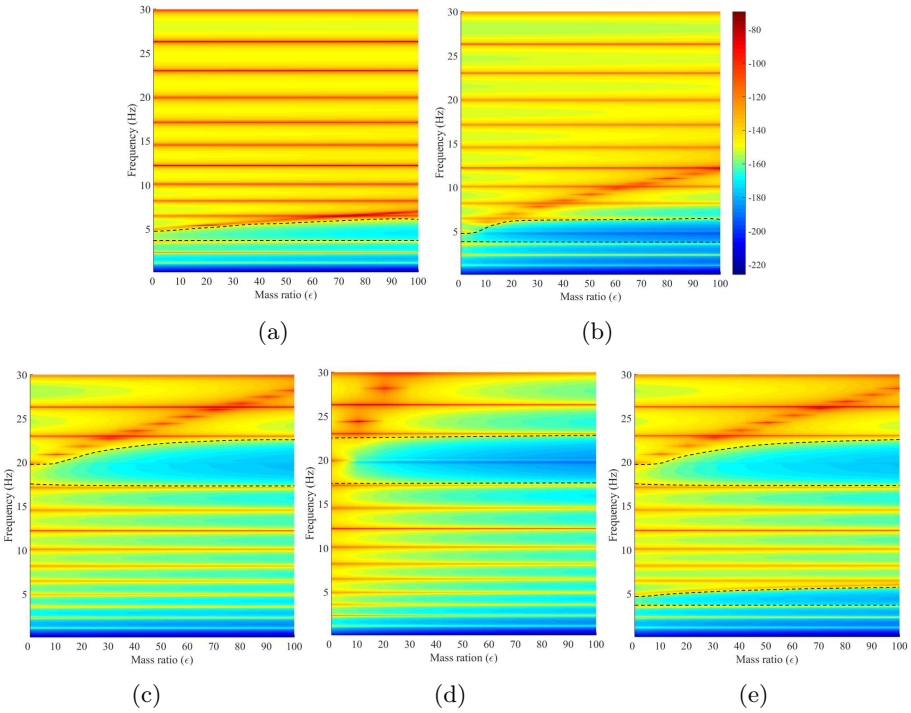

Fig. 6: Bandgap formation map: (a) Metamaterial beam with designed LR bandgap at 4.92Hz; (b) Rainbow metamaterial beam with designed LR bandgap around 4.92Hz; (c) Metamaterial beam with designed LR bandgap at 19.92Hz; (d) Rainbow metamaterial beam with designed LR bandgap around 19.92Hz; (c) Multi-frequency metamaterial beam with tuned frequencies at 4.92 and 19.92Hz.

In brief, one can expect that low-frequency bandgaps will have a relatively small structural response in the bandwidth and its convergence with less mass ratio and that high-frequency bandgaps will have a wider gap, but a bigger mass ratio is needed for the convergence. Indeed, it is inevitable that any damping in the structure will limit the extent of vibration reduction and affect the responses. This, however, was not examined in this study. It is expected that this dynamic characteristic of the metamaterials would differ for different combinations of boundary conditions and low resonator values because the modal parameters will be different.

4.2 Experimental application

Cable experimental measured inertance responses are compared with the numerical model based on the spectral element method (SEM) [33, 37, 38] and

on Modal analysis technique applied in this paper. The digital twin is a computerized model of a physical system that represents all functional features and links with the working elements [34]. This section is devoted to validating the numerical model employed here and building the digital twin cable, which will be a reference model for the physical–virtual convergence. The cable's structural parameters used to compute the virtual cable were estimated from the experimental data using Bayesian identification and Markov Chain Monte Carlo methods, briefly described in Appendix A. Further analysis used the virtual cable to investigate its vibration mitigation and the bandgap formation.

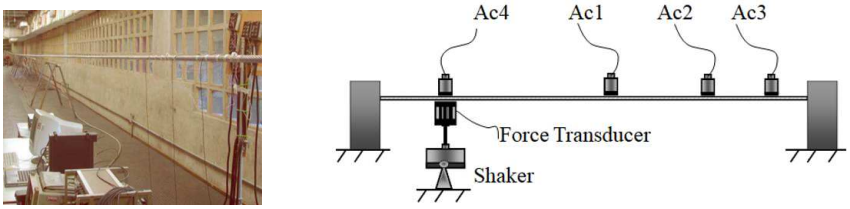

Fig. 7: Experimental set-up: general overview of the CEPEL's laboratory span (left) and schematic experimental set-up(right) [32, 33].

The experimental test illustrated in Fig. 7 was performed at the laboratory span of the Electric Power Research Center (CEPEL). The simply-supported cable under analysis is an ACSR Grosbeak with a nominal diameter of $D = 25.15$ mm, a mass per unit length of $\rho A = 1.3027$ kg/m, and the length of $L = 51.950$ m. The estimated cable's Young's Modulus was $E = 2.01$ GPa, as given in Appendix A, and density of $\rho = 3000$ kg/m^3. In the experimental tests, the tensile load was set at 1680 kgf, about 19% of the Grosbeak rated tensile strength. The cable was excited by an electrodynamic shaker at 1.606 m from the support and measured with four accelerometers nominated Ac4, Ac1, Ac2, and Ac3, placed at 1.606 m, 26 m, 34 m, and 39 m, respectively. The force transducer used is a Bruel-Kjäer-model 8230-002, and the accelerometers are IEPE Bruel-Kjäer-model Deltatron 4519-001 with 1 gr mass (more details of experimental set up in [32, 33]).

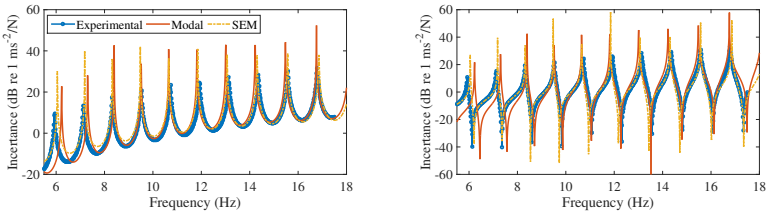

Fig. 8: Comparison of experimental inertance response to numerical response calculated using SEM and Modal Analyse. Inertance response are obtained at accelerometer Ac3 (LHS) and at the point of the accelerometer Ac4 (RHS).

Figure 8 is the comparison of numerical response calculated using SEM and Modal Analysis, with the experimental inertance response of the cable without attachments, all obtained on accelerometer Ac3 and Ac4. The curves show a good approximation among them, and the numerical models did not consider any damping, which explains the sharp resonance picks. The vibration control simulation was performed by the constructed local resonant absorbers using the digital twin of the cable. Designed resonators vibrated at the tuned frequencies of 9.51 and 15.48 Hz, attached uniformly along the cable within 1.73 m resulting in a total of 28% of mass ratio

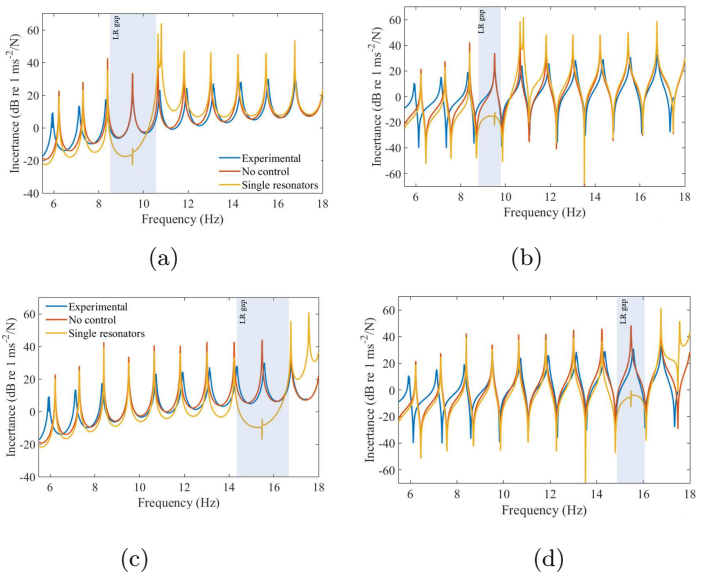

Fig. 9: Experimental and numerical inertances with and without control. Metamaterial beam with designed LR bandgap at 9.51 Hz obtained at accelerometers Ac3 (a) and Ac4 (b). Metamaterial beam with designed LR bandgap at 15.48Hz obtained at accelerometers Ac3 (c) and Ac4 (d)

.

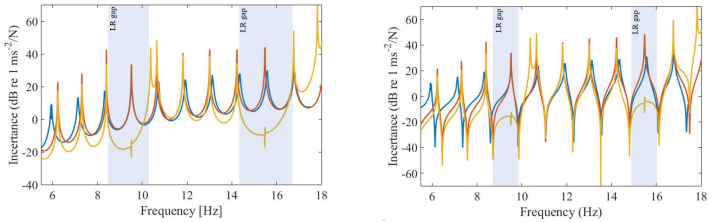

Fig. 10: Experimental and numerical inertances with and without control. Metamaterial beam with designed LR bandgap at 9.51 Hz and 15.48Hz obtained at accelerometers Ac3 (LHS) and Ac4 (RHS).

Figures 9a and 9b are, respectively, the inertance responses obtained at accelerometers Ac3 and Ac4. The images show the plain cable experimental response (without attachments), numerical inertance for the plain virtual cable, and metamaterial cable with designed LR bandgap at 9.51 Hz. Herein, only the metamaterial was applied given the the existence of ADV, known as Stocksbridge, which commonly works in two frequency ranges. Figures 9c and 9d show the plain cable experimental response on the Ac3 and Ac4

points and the numerical response of the plain virtual cable and the metamaterial with a tuned frequency at 15.48 Hz. Assuming the mass ratio of 28%, a bandgap was generated and isolated the vibration at desired frequencies. The shift frequency effect impacted the closest mode shapes, slightly increasing the amplitude and inducing other resonance points. Aside from this disorder, the cable's dynamic maintained its modal characteristic. By implying multiple frequencies, as shown in Fig 10, two open bandgaps were formed simultaneously.

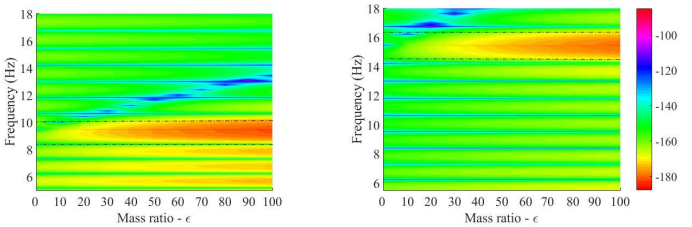

Fig. 11: Bandgap formation map of the metamaterial cable with designed LR bandgap at 9.51Hz (LHS) and at 15.48Hz (RHS).

The bandwidth is determined by the ratio of the total mass of the absorbers related to the plain cable mass, as demonstrated in section 4.1. For the cable application, mass ratio versus bandgap formation is displayed in g 11. Stabilization of the bandwidth occurred around 30% for the LR gap set at 9.51Hz and 45% at 15.48Hz. From the relation $m_p = mL/S$, it is easy to calculate the number of resonators needed. Therefore, 28% of mass ratio corresponds to S=30 of resonators periodically attached to the cable, and $\epsilon = 45\%$ is near 47 resonators.

5 Conclusion

This work investigated broadband vibration mitigation employing a metamaterial and rainbow metamaterial beam under tensile load. We calculated the theory for bandgap estimation proposed in [12], which was extended to a beam under tensile load application and presented for a multi-frequency application. Local resonant bandgap formation for simple and multiple frequencies was directly influenced by the mass ratio, which saturated, and could not widen the band above a certain mass. When we wished to widen the gap, the concept of rainbow metamaterial proved a solid alternative. The results show the concept of rainbow metamaterial through the beam's receptance responses, and the bandgap map shows the gain when using the rainbow metamaterial, which influences the bandwidth and the shifting resonant frequency effects. Bandgap formation related to the mass ratio was also explored. In lower modes, the bandgaps presented a small structural response in the bandwidth and it

converged with less mass ratio while, for higher modes, the bandgaps were wider but a bigger mass ratio was needed. We expected that this dynamic feature of the metamaterials would differ for different combinations of boundary conditions and low resonators values because the modal parameters were different.

For an application study case, we considered a cable metamaterial. The digital twin cable was derived from a physical cable installed at CEPEL's laboratory, representing all functional features and links with the working system. The cable's structural parameters used to computerize the digital model were estimated from the experimental data by Bayesian identification theory. The virtual twin of the cable was used to investigate its vibration characteristics, mitigation, and bandgap formation. This proved to be a powerful model to monitor and design the optimum vibration control system for the cable.

Acknowledgments. The authors declare that they have no conflict of interest.

M.R.Machado would like to acknowledge the support received through the Fundação de Apoio a Pesquisa do Distrito Federal-FAPDF (Grants no. 00193-00000766/2021-71 and 00193-00000826/2021-55).

This manuscript has received the recommendation of DSTA 2021 Committee.

This manuscript has no data availability.

Appendix A Cable parameter estimation

The process of building a computational model ($\mathcal{M}$) is considered to describe the physical system ($\mathcal{B}$). In addition, a set of measurements (y) is known and the structuring process occurs from the identification of the parameters' vector of interest (θ). Where y and θ are modelled as a random variable, the model's predictive response is given by $y^m = y^m(\theta)$. The *a posterior* probability distribution function(PDF), which relates the PDFs of the experimental data to the vector of parameters of interest $\pi(\theta|y)$, is based on the Bayes theorem expressed in terms of probability distributions, and takes the following form

$$\pi(\theta|y) = \frac{\pi(y|\theta)\pi(\theta)}{\pi(y)} \tag{A1}$$

where $\pi(y|\theta)$ represents the system's likelihood function, $\pi(\theta)$ *prior* PDF, and $\pi(y)$ is the PDF associated with the experimental data. The information about the likelihood PDF can be obtained using a particular model of observation of the system. It is considered that the relationship between the observed data (y) and the predictions of the ($y(\theta)^m$) model can be described from an observation model with additive noise (ν) as $y^{exp} = y(\theta)^m + \nu$. The additive noise describes the difference between an experimental observation and the prediction of the model, represented by a random vector. Therefore, given that y, θ and ν are random variables will be related to a joint PDF $\pi(y, \theta, \nu)$. By considering that

the noise is stationary, Gaussian with known variance σ_ν^2, then the likelihood function can be represented as

$$\pi(y^{exp}|\theta_i) = \frac{1}{(2\pi)^{n/2}\,\sigma_\nu^n} exp\left(-\frac{1}{2}\frac{(y^{exp} - y^m\,(\theta_i))^T\,(\,y^{exp} - y^m\,(\theta_i))}{\sigma_\nu^2}\right) \quad \text{(A2)}$$

which corresponds to the probability of having measured data y^{exp} given a specific model $y(\theta)^m$, defined by the parameter set θ. To obtain information about the unknown parameters, we used the Monte Carlo Markov Chain from the UQLab toolbox [39].

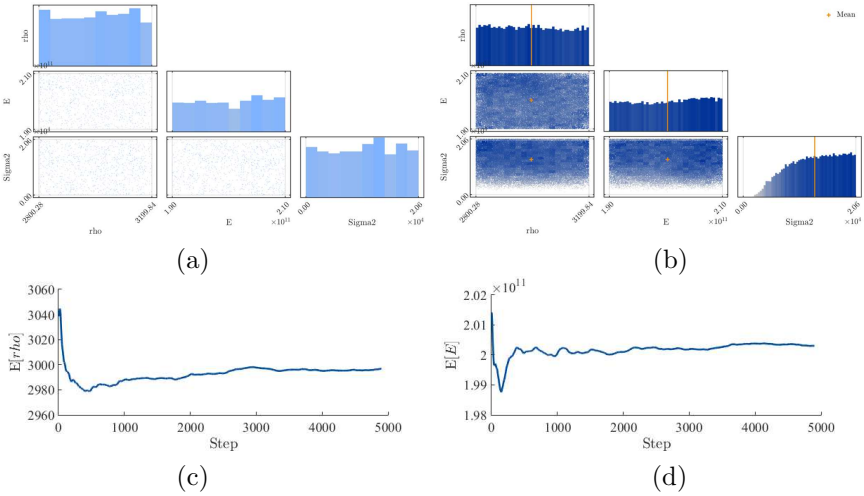

Fig. A1: Bandgap formation map of the metamaterial cable with designed LR bandgap at 9.51Hz (LHS) and 15.48Hz (RHS).

In the estimation operated with 20 chains, each one contained 5000 samples. Prior distribution of Young's modulus and mass were assumed as uniform U_ρ(2.8e3, 3.2e3) and U_E(190e9, 210e9), respectively. Figures A1(a-b) are the scatterplots of prior and posterior distribution related to their respective discrepancy parameter $pi(\sigma^2)$ of each parameter. Figures A1(c-d) are the convergence graph of the expected parameter values over all chains. Results show that Young's modulus converges to $E = 2.01$GPa and density to 3000 kg/m^3 estimated from the experimental data.

References

[1] Meirovitch, L.: Fundamentals of vibrations. In McGraw-Hill, 2001.

[2] Sugino, C., Xia, Y., Leadenham, S., Ruzzene, M., and Erturk, A. A general theory for bandgap estimation in locally resonant metastructures. Journal of Sound and Vibration, 406, (2017). https://doi.org/10.1016/j.jsv.2017.06.004

[3] Rao, S. S., Mechanical Vibrations, Sixth Edition in SI Units, Pearson, (2018).

[4] Sun H, Du X, Pai PF. Theory of Metamaterial Beams for Broadband Vibration Absorption. Journal of Intelligent Material Systems and Structures. 2010;21(11):1085-1101. doi:10.1177/1045389X10375637

[5] Metamaterial market analysis, by product (electromagnetic, terahertz, photonic, tunable, frequency selective surface, non-linear), by application, end-use, and segment forecasts, 2018 - 2025. 2018. https://www.grandviewresearch.com/industry-analysis/metamaterials-market Accessed in 18/11/2021.

[6] Valipour, A., Kargozarfard, M. H., Rakhshi, M., Yaghootian, A., and Sedighi, H. M. (2021). Metamaterials and their applications: An overview. Proceedings of the Institution of Mechanical Engineers, Part L: Journal of Materials: Design and Applications.

[7] Dalela, S., Balaji, P. S., and Jena, D. P. (2021). A review on application of mechanical metamaterials for vibration control. Mechanics of Advanced Materials and Structures, 1–26. https://doi.org/10.1080/15376494.2021.1892244

[8] J.Q. Sun, M.R. Jolly, M.A. Norris, Passive, adaptive and active tuned vibration absorbers—a survey, Journal of Vibration and Acoustics 117 (1995) 234–242

[9] Y. Xiao, J. Wen, X. Wen, Flexural wave band gaps in locally resonant plates with periodically attached spring-mass resonators, J. Phys. D: Appl. Phys. 45 (19) (2012) 195401.

[10] Dianlong Yu, Yaozong Liu, Honggang Zhao, Gang Wang, and Jing Qiu, Flexural vibration band gaps in Euler-Bernoulli beams with locally resonant structures with two degrees of freedom, Phys. Rev. B 73, 064301, 2006.

[11] Xiao, Y., Wen, J., Yu, D., and Wen, X. (2013). Flexural wave propagation in beams with periodically attached vibration absorbers: Band-gap behavior and band formation mechanisms. Journal of Sound and Vibration, 332(4), 867–893. https://doi.org/10.1016/j.jsv.2012.09.035

[12] Sugino, C., Xia, Y., Leadenham, S., Ruzzene, M., and Erturk, A. (2017). A general theory for bandgap estimation in locally resonant metastructures. Journal of Sound and Vibration, 406. https://doi.org/10.1016/j.jsv.2017.06.004

[13] Sugino, C., Leadenham, S., Ruzzene, M., and Erturk, A. (2016). On the mechanism of bandgap formation in locally resonant finite elastic metamaterials. Journal of Applied Physics, 120(13). https://doi.org/10.1063/1.4963648

[14] Miranda Jr., E. J. P., and Dos Santos, J. M. C. (2019). Flexural wave band gaps in multi-resonator elastic metamaterial Timoshenko beams. Wave Motion, 91, 102391. https://doi.org/10.1016/j.wavemoti.2019.102391

[15] D. Yu, Y. Liu, G. Wang, H. Zhao, J. Qiu, Flexural vibration band gaps in Timoshenko beams with locally resonant structures, J. Appl. Phys. 100 (124901) (2006) 1–5, http://dx.doi.org/10.1063/1.2400803.

[16] Y. Xiao, J. Wen, X. Wen, Broadband locally resonant beams containing multiple periodic arrays of attached resonators, Phys. Lett. A 376 (16) (2012) 1384–1390, http://dx.doi.org/10.1016/j.physleta.2012.02.059

[17] Xia, Y., Ruzzene, M. and Erturk, A. Bistable attachments for wideband nonlinear vibration attenuation in a metamaterial beam. Nonlinear Dyn 102, 1285–1296 (2020). https://doi.org/10.1007/s11071-020-06008-4

[18] Cveticanin, L., Zukovic, M. and Cveticanin, D. Influence of nonlinear subunits on the resonance frequency band gaps of acoustic metamaterial. Nonlinear Dyn 93, 1341–1351 (2018). https://doi.org/10.1007/s11071-018-4263-5

[19] He, Jimin and Fu, Z.-F. (n.d.). Modal Analysis. Butterworth-Heinemann, Oxford, UK, 2001.

[20] P. Hagedorn, On the computation of damped wind-excited vibrations of overhead transmission lines, J. Sound Vib. 83 (1982) 253–271

[21] M.S. Dhotarad, N. Ganesan, B.V.A. Rao, Transmission line vibrations, J. Sound Vib. 60 (1978) 217–237.

[22] M. Irvine, H.Irvine, Cable Structures, Dover Publications, New York (NY), 1992.

[23] Taut helical strand bending stiffness. Available from:http://imechanica.org/files/Cardou-art-2006.pdf..

[24] K. Spak, G. Agnes, D. Inman, Parameters for modeling stranded cables as structural beams, Exp. Mech. 54 (9) (2014) 1613–1626.

[25] K. Spak, G. Agnes, D. Inman, Modeling vibration response and damping of cables and cabled structures, J. Sound Vib. 336 (2015) 240–256.

[26] Barry, O., Long, R., and Oguamanam, D. C. D. (2017). Simplified Vibration Model and analysis of a single-conductor transmission line with dampers. Proceedings of the Institution of Mechanical Engineers, Part C: Journal of Mechanical Engineering Science, 231(22), 4150–4162. https://doi.org/10.1177/0954406216660736

[27] Xia, Y., Ruzzene, M., and Erturk, A. (2020). Bistable attachments for wideband nonlinear vibration attenuation in a metamaterial beam. Nonlinear Dynamics, 102(3), 1285–1296. https://doi.org/10.1007/s11071-020-06008-4

[28] Cveticanin, L., Zukovic, M., and Cveticanin, D. (2018). Influence of nonlinear subunits on the resonance frequency band gaps of acoustic metamaterial. Nonlinear Dynamics, 93(3), 1341–1351. https://doi.org/10.1007/s11071-018-4263-5

[29] Zhou, W., Wu, B., Su, Y., Liu, D., Chen, W., and Bao, R. (2021). Tunable flexural wave band gaps in a prestressed elastic beam with periodic smart resonators. Mechanics of Advanced Materials and Structures, 28(3), 221–228. https://doi.org/10.1080/15376494.2018.1553261

[30] Celli, P., Yousefzadeh, B., Daraio, C., and Gonella, S. (2019). Bandgap widening by disorder in rainbow metamaterials. Applied Physics Letters, 114(9). https://doi.org/10.1063/1.5081916

[31] Hu, G., C. M. Austin, A., Sorokin, V., and Tang, L. (2021). Metamaterial beam with graded local resonators for broadband vibration suppression. Mechanical Systems and Signal Processing, 146, 106982. https://doi.org/10.1016/j.ymssp.2020.106982

[32] Castello, D. A., and Matt, C. F. T. (2011). A validation metrics based model calibration applied on stranded cables. Journal of the Brazilian Society of Mechanical Sciences and Engineering, 33(4), 417–427. https://doi.org/10.1590/S1678-58782011000400005

[33] Machado, M. R., Dutkiewicz, M., Matt, C. F. T., and Castello, D. A. (2020). Spectral model and experimental validation of hysteretic and aerodynamic damping in dynamic analysis of overhead transmission conductor. Mechanical Systems and Signal Processing, 136, 106483. https://doi.org/10.1016/j.ymssp.2019.106483

[34] Y. Chen, Integrated and Intelligent Manufacturing: Perspectives and Enablers, Engineering, vol. 3, pp. 588–595, Oct. 2017.

[35] Fuller, A., Fan, Z., Day, C., and Barlow, C. (2020). Digital Twin: Enabling Technologies, Challenges and Open Research. IEEE Access, 8(June), 108952–108971. https://doi.org/10.1109/ACCESS.2020.2998358

[36] Y. Zheng, S. Yang, and H. Cheng, "An application framework of digital twin and its case study," Journal of Ambient Intelligence and Humanized Computing, vol. 10, pp. 1141–1153, June 2018.

[37] Dutkiewicz, M., and Machado, M. (2019). Spectral element method in the analysis of vibrations of overhead transmission line in damping environment. Structural Engineering and Mechanics, 71(3), 291–303. https://doi.org/10.12989/SEM.2019.71.3.291

[38] Dutkiewicz, M., Machado, M. R. (2019). Measurements in Situ and Spectral Analysis of Wind Flow Effects on Overhead Transmission Lines. Sound and Vibration, 53(4), 161–175.

[39] Stefano Marelli and Bruno Sudret,UQLab: A Framework for Uncertainty Quantification in MATLAB, In The 2nd International Conference on Vulnerability and Risk Analysis and Management (ICVRAM 2014), University of Liverpool, United Kingdom, July 13-16, 2014, pp. 2554–2563. 10.1061/9780784413609.257

[40] Zhong, R., Pai, P.F., Zong, Z., Deng, H., and Ruan, X., Metamaterial I-Girder for Vibration Absorption of Composite Cable-Stayed Bridge, Journal of Engineering Mechanics, Volume 144 Issue 7 - July 2018

[41] Singleton, L., Cheer, J., and Daley,S., Design of a Resonator-Based Metamaterial for Broadband Control of Transverse Cable Vibration, In Proceedings of the 23rd International Congress on Acoustics : integrating 4th EAA Euroregio 2019 : 9-13 September 2019 in Aachen, Germany.